


 Cite this: *Chem. Commun.*, 2023, 59, 13767

 Received 6th September 2023,  
 Accepted 24th October 2023

DOI: 10.1039/d3cc04409b

rsc.li/chemcomm

**Converting CO<sub>2</sub> to liquid (C<sub>5+</sub>) hydrocarbons remains a significant hurdle. Our study shows that CoFe/HZSM-5 boosts C<sub>5+</sub> selectivity to 73.4%, up from 59% for Fe/HZSM-5. This study highlights the pivotal roles of zeolite acidity and catalyst proximity in this improvement. These insights pave the way for more effective CO<sub>2</sub> utilization.**

The hydrogenation of CO<sub>2</sub> into valuable chemicals such as aromatics and olefins presents an effective approach for addressing the rising CO<sub>2</sub> levels, transforming the greenhouse gas into beneficial resources. This process holds potential in mitigating CO<sub>2</sub> emissions and converting CO<sub>2</sub> into a sought-after commodity.<sup>1</sup>

Despite challenges such as CO<sub>2</sub>'s inert nature and high energy barriers for C–C coupling,<sup>2</sup> there are two main approaches for CO<sub>2</sub> hydrogenation into long-chain hydrocarbons: the methanol-mediated (CO<sub>2</sub>-MeOH) route and the CO<sub>2</sub> modified Fischer-Tropsch synthesis (CO<sub>2</sub>-FTS) route. The CO<sub>2</sub>-MeOH route, despite yielding a higher proportion of low carbon olefins or liquid (C<sub>5+</sub>) hydrocarbons, has limitations like low CO<sub>2</sub> conversion and increased CO selectivity.<sup>3,4</sup> The CO<sub>2</sub>-FTS route involves CO<sub>2</sub> transformation into CO intermediates through reverse water-gas shift (RWGS) and further conversion to C<sub>2+</sub> products *via* the FTS process.<sup>5</sup> Co- and Fe-based catalysts are widely used in the FTS route.<sup>6</sup> While the Fe-based catalysts are effective for both RWGS and FTS processes, the Co-based catalysts often show inefficiency due to their lack of RWGS reactivity.<sup>7</sup> Enhancing the performance of the Co-based catalysts with active sites for the RWGS reaction improves the overall process. Specific studies have seen success by integrating noble metals or alkali metals into the Co-based

## Bifunctional CoFe/HZSM-5 catalysts orient CO<sub>2</sub> hydrogenation towards liquid hydrocarbons†

 Kai Wang,<sup>ab</sup> Na Liu,<sup>ab</sup> Jian Wei,<sup>id</sup>\*<sup>a</sup> Yang Yu,<sup>ab</sup> Jixin Zhang,<sup>a</sup>  
 Joshua Iseoluwa Orege,<sup>ab</sup> Lifei Song,<sup>a</sup> Qingjie Ge<sup>id</sup><sup>a</sup> and Jian Sun<sup>id</sup>\*<sup>a</sup>

catalysts, leading to a reduced CO<sub>2</sub> conversion rate but augmented production of long-chain hydrocarbons.<sup>8</sup>

In recent years, researchers have developed multi-active-site synergistic catalysts by pairing metal catalysts with zeolites for CO<sub>2</sub> hydrogenation.<sup>5</sup> Zeolites, unique in their topological structures and acidic properties, aid in hydrocarbon reactions like oligomerization and isomerization.<sup>9</sup> After CO<sub>2</sub> transforms into olefins *via* the metal catalyst, it is further converted to higher carbon hydrocarbons on the zeolites.<sup>10</sup> The ZSM-5 zeolite framework consists of interconnected 10-membered rings, creating a three-dimensional microporous channel structure.<sup>11</sup> These channels provide a large surface area and space for molecular diffusion,<sup>12,13</sup> making ZSM-5 more resistant to coking compared to other zeolites due to its pore system constraints.<sup>14</sup>

In our recent work, we found that CoFe alloy carbide catalysts excel in converting CO<sub>2</sub> to olefins,<sup>15</sup> which are key intermediates in the CO<sub>2</sub>-FTS route. Enhancing olefin selectivity is a strategic move, as it inherently augments the selectivity of C<sub>5+</sub> hydrocarbons in subsequent reactions. CoFe alloy catalysts, with their exemplary capability to catalyse the transformation of CO<sub>2</sub> into olefins, can bolster the system's proficiency in CO<sub>2</sub> conversion to C<sub>5+</sub> hydrocarbons.<sup>16</sup> With this premise, our explorations have delved into the integration of ZSM-5 zeolites, exhibiting varied acidity characteristics, with CoFe alloy catalysts. This paper seeks to present a comprehensive study of the CO<sub>2</sub> hydrogenation performance steered by this tandem catalytic system and decipher the underlying mechanisms influenced by zeolite acidity and the nuanced interplay between the zeolite and metal catalyst.

The crystal structures of each component in the tandem catalyst system were characterized using X-ray diffraction (XRD) analysis. The fresh CoFe catalyst displayed distinct peaks at  $2\theta = 36.8^\circ$  and  $48.5^\circ$ , matching the CoFe<sub>2</sub>O<sub>4</sub> phase (Fig. S1, PDF #22-1086, ESI†),<sup>17</sup> while the spent catalyst revealed (Co<sub>x</sub>Fe<sub>1-x</sub>)<sub>5</sub>C<sub>2</sub> alloy carbide, the key active centre for CO<sub>2</sub> hydrogenation (Fig. S2, ESI†). These results align with our previous studies on CoFe catalysts.<sup>18</sup> Hydrothermally-synthesized HZSM-5 zeolites (see the details in the ESI†) are denoted as HZ-5(X), where X

<sup>a</sup> Dalian National Laboratory for Clean Energy, Dalian Institute of Chemical Physics, Chinese Academy of Sciences, Dalian 116023, China.  
 E-mail: weijian@dicp.ac.cn, sunj@dicp.ac.cn

<sup>b</sup> University of Chinese Academy of Sciences, Beijing 100049, China

† Electronic supplementary information (ESI) available. See DOI: <https://doi.org/10.1039/d3cc04409b>





**Fig. 1** (a) XRD patterns of HZSM-5 zeolites; (b)  $\text{NH}_3$ -TPD curves of HZSM-5 zeolites; (c) Py-IR spectra of HZSM-5 zeolites recorded after the removal of weakly adsorbed pyridine by evaporation at 200 °C; (d) SEM diagram of HZ-5(40).

corresponds to the  $\text{SiO}_2/\text{Al}_2\text{O}_3$  ratio values: 40, 80, 160, 320, and 640. (A sample with a ratio of 20 was tested but quickly deactivated (Fig. S3, ESI<sup>†</sup>). Thus, we emphasized samples with higher ratios.) Their XRD patterns (Fig. 1a) showed peaks aligning closely with standard ZSM-5 (PDF #44-0003), confirming their high crystallinity and well-defined MFI topology.

The textural properties of CoFe were explored using  $\text{N}_2$  adsorption-desorption experiments, revealing a mesoporous structure (Table S1, ESI<sup>†</sup>). The textural properties of HZSM-5 zeolites were investigated through  $\text{N}_2$  adsorption-desorption experiments and scanning electron microscopy (SEM). The  $\text{N}_2$  adsorption-desorption curves and textural properties of HZSM-5 zeolites with different  $\text{SiO}_2/\text{Al}_2\text{O}_3$  ratios are shown in Fig. S4 (ESI<sup>†</sup>) and Table 1. All zeolites exhibited typical Type I isotherms, indicating their microporous structures. Moreover, variations in the  $\text{SiO}_2/\text{Al}_2\text{O}_3$  ratio had a negligible influence on the structural properties of ZSM-5, as evident from the specific surface area and total pore volume. The SEM image in Fig. 1d reveals that the HZ-5(40) crystals are approximately 2–4  $\mu\text{m}$  in size and exhibit a smooth surface, consistent with the zeolites having other  $\text{SiO}_2/\text{Al}_2\text{O}_3$  ratios (Fig. S4, ESI<sup>†</sup>).

The acidity of HZSM-5 zeolites is pivotal in influencing the reactivity of tandem catalysts and hydrocarbon product

selectivity. By employing  $\text{NH}_3$ -temperature-programmed desorption ( $\text{NH}_3$ -TPD) and pyridine adsorption infrared (Py-IR) techniques, the acidic properties were systematically characterized. The  $\text{NH}_3$ -TPD results showed desorption peaks at around 200 and 450 °C, representing weak and strong acidic sites, which decreased in intensity as the  $\text{SiO}_2/\text{Al}_2\text{O}_3$  ratio increased from 40 to 640. Concurrently, the Py-IR spectra indicated a corresponding decline in Brønsted and Lewis acid site (BAS and LAS) concentrations, from 61.90 to 3.85  $\mu\text{mol g}^{-1}$  for the BAS and 117.14 to 46.72  $\mu\text{mol g}^{-1}$  for the LAS (Table 1). Both methods consistently suggest that increasing the  $\text{SiO}_2/\text{Al}_2\text{O}_3$  ratio leads to reduced acid strength and concentration, attributable to the decreased aluminium content.

The CoFe alloy catalyst and HZSM-5 with different acidic properties were combined through particle mixing in a mass ratio of CoFe:HZSM-5 = 1:2 unless otherwise stated. After reducing and pretreating the catalyst at 350 °C under a  $\text{H}_2$  atmosphere for 8 hours, its  $\text{CO}_2$  hydrogenation performance was evaluated (Fig. 2a and b). The individual CoFe alloy catalyst achieved a  $\text{CO}_2$  conversion rate of 39.0% with a CO selectivity of 11.3%, primarily producing olefins from  $\text{CO}_2$  hydrogenation. It should be noted that both the CoFe and Fe catalysts used in this study were modified with sodium (Na) to enhance their catalytic performance,<sup>19</sup> enhancing their catalytic performance.  $\text{CH}_4$  and straight-chain paraffins constituted a minor fraction of the hydrocarbon products, with the negligible formation of aromatics or iso-paraffins. When the CoFe alloy catalyst was combined with the HZ-5(40) zeolite, the tandem catalyst shifted the hydrocarbon profile significantly—olefins within  $\text{C}_{5+}$  fell from 68.5% to 1.0%, while aromatics and iso-paraffins surged from 0% and 11.3% to 73.1% and 18.2%, respectively. Essentially, CoFe funneled  $\text{CO}_2$  through  $\text{CO}_2$ -FTS to olefins, further transformed by HZ-5(40) into aromatics and iso-paraffins. Against a conventional Fe/HZ-5(40) system, CoFe/HZ-5(40) maintained a similar  $\text{CO}_2$  conversion rate but reduced CO selectivity, most notably elevating  $\text{C}_{5+}$  selectivity from 59.0% to 71.5%. This is attributed to CoFe's exceptional ability in  $\text{CO}_2$ -to-olefins conversion. We also tested the time on stream stability of CoFe/HZ-5(40) for over a 24 hour period and observed that the catalyst exhibited minimal performance degradation after achieving stability (Fig. S6, ESI<sup>†</sup>).

To probe the CoFe/HZSM-5 tandem system's synergistic effect, we studied zeolite acidity, proximity, and the mass ratio between the components, and their influence on the catalytic system. Zeolite acidity affects aromatization and isomerization, causing different tandem system performances (Fig. 2a and b).

**Table 1** Textural and acidic properties of HZSM-5 zeolites

| Zeolite   | $\text{SiO}_2/\text{Al}_2\text{O}_3^a$ | $S_{\text{BET}}^b$ ( $\text{m}^2 \text{g}^{-1}$ ) | $V_{\text{pore}}^c$ ( $\text{cm}^3 \text{g}^{-1}$ ) | $C_{\text{BAS}}^d$ ( $\mu\text{mol g}^{-1}$ ) | $C_{\text{LAS}}^e$ ( $\mu\text{mol g}^{-1}$ ) | $C_{\text{BAS}}/C_{\text{LAS}}$ ratio |
|-----------|--|---|---|---|---|---------------------------------------|
| HZ-5(40)  | 45.8                                   | 423.3   | 0.253   | 61.90   | 177.14  | 0.35                                  |
| HZ-5(80)  | 91.4                                   | 418.3   | 0.197   | 32.99   | 111.38  | 0.30                                  |
| HZ-5(160) | 187.8                                  | 402.5   | 0.190   | 22.58   | 93.13   | 0.24                                  |
| HZ-5(320) | 353.5                                  | 390.4   | 0.196   | 8.68  | 72.52   | 0.12                                  |
| HZ-5(640) | 682.4                                  | 368.4   | 0.283   | 3.85  | 46.72   | 0.12                                  |

<sup>a</sup>  $\text{SiO}_2/\text{Al}_2\text{O}_3$ :  $\text{SiO}_2/\text{Al}_2\text{O}_3$  molar ratio by XRF analysis. <sup>b</sup>  $S_{\text{BET}}$ : specific surface area calculated by the BET method. <sup>c</sup>  $V_{\text{pore}}$ : total pore volume. <sup>d</sup>  $C_{\text{BAS}}$ : concentrations of the Brønsted acid site calculated using the Lambert-Beer equation. <sup>e</sup>  $C_{\text{LAS}}$ : concentrations of the Lewis acid site calculated using the Lambert-Beer equation.



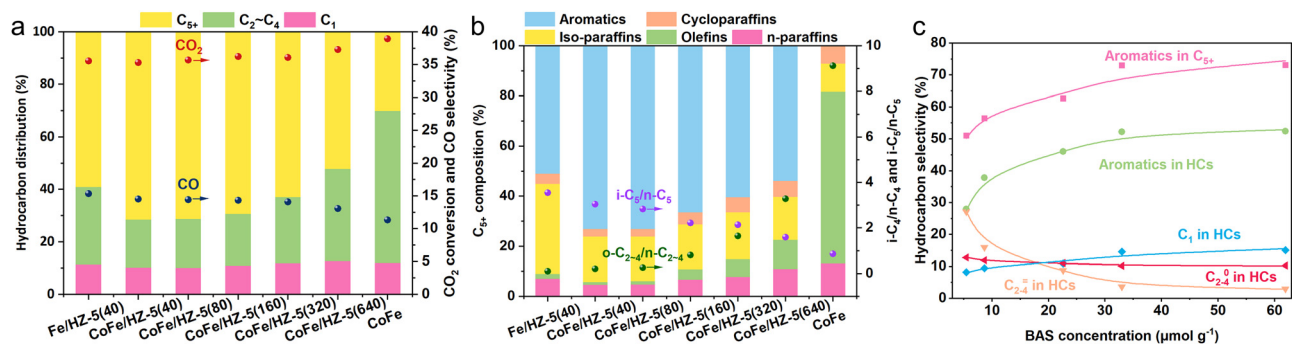


Fig. 2 Hydrocarbon distribution (a) and  $C_{5+}$  composition (b) in the case of  $CO_2$  hydrogenation over various catalysts; (c) effect of the BAS concentration on the performance of composite catalysts. N- $C_{5+}$  means  $C_{5+}$  hydrocarbons other than aromatics.  $C_{2-4}$  and  $C_{2-4}$  denote the paraffins and olefins of  $C_2-C_4$  hydrocarbons, respectively. Reaction conditions:  $320\text{ }^\circ\text{C}$ ,  $3.0\text{ MPa}$ ,  $H_2/CO_2/N_2 = 72/24/4$  (vol%),  $4000\text{ mL g}_{\text{cat}}^{-1}\text{ h}^{-1}$ , time on steam = 14 h.

The BAS, the active site for aromatization, is related to HZSM-5 aromatization capacity.<sup>20</sup> We compared the performances of catalysts with different BAS concentrations using Py-IR technology (Fig. 2c). Increasing the BAS concentration from  $3.85$  (HZ-5(640)) to  $22.58$  (HZ-5(160))  $\mu\text{mol g}^{-1}$  boosts aromatic selectivity in  $C_{5+}$  hydrocarbons from  $53.8\%$  to  $73.0\%$ . However, further increases have diminishing returns, suggesting an upper limit for the BAS concentration in promoting aromatic selectivity. At a peak BAS concentration of  $61.90\text{ }\mu\text{mol g}^{-1}$ , we achieved the highest  $C_{5+}$  aromatic selectivity of  $73.1\%$ . As the BAS concentration increased,  $C_2-C_4$  olefin selectivity dropped from  $27.3\%$  to  $2.8\%$ , while  $C_2-C_4$  paraffin selectivity rose from  $8.2\%$  to  $15.1\%$ , reducing the olefin/paraffin ratio from  $3.3$  to  $0.2$ . These changes indicate that the BAS also facilitates olefin hydrogenation, thus increasing paraffin selectivity. Consequently, the BAS concentration is pivotal for selective  $CO_2$  aromatization by the CoFe/HZSM-5 system.

In the CoFe/HZSM-5 catalyst system, the spatial proximity between CoFe and the zeolite is pivotal for their synergistic effects on  $CO_2$ -to- $C_{5+}$  hydrocarbon conversion.<sup>21</sup> Three configurations—dual bed, particle mixing, and powder mixing—were used to modulate this spatial relationship (Fig. 3a and b). The dual bed configuration yielded a  $34.1\%$   $CO_2$  conversion rate and  $15.9\%$  CO selectivity, with  $C_{5+}$  hydrocarbons comprising  $67.9\%$  and aromatics making up  $62.4\%$  within  $C_{5+}$ . Particle mixing enhanced the  $CO_2$  conversion to  $35.3\%$  and lowered CO selectivity to  $14.5\%$ , while increasing the selectivity for  $C_{5+}$  hydrocarbons and aromatics within  $C_{5+}$  to  $71.5\%$  and  $73.1\%$ , respectively. This indicates that reducing the CoFe/HZSM-5 distance promotes olefin diffusion to HZSM-5, benefiting  $C_{5+}$  formation. However, close proximity lowered  $CO_2$  conversion to  $27.3\%$  and raised CO selectivity. This was probably due to Na ions moving from CoFe to the zeolite acidic sites, poisoning them and altering the catalyst's properties.<sup>5,22</sup>

In the CoFe/HZSM-5 system, the product composition is notably affected by the CoFe/HZSM-5 mass ratio (Fig. 3c and d). Increasing the CoFe/HZSM-5 mass ratio from  $0.2$  to  $0.8$  elevates the  $CO_2$  conversion rate from  $32.7\%$  to  $41.6\%$ , while CO selectivity decreases from  $18.1\%$  to  $9.4\%$ . Alongside this, the selectivity towards  $CH_4$  shows an increasing trend, scaling from  $11.2\%$  to  $15.6\%$ , as the CoFe/HZ-5(40) mass ratio ascends from



Fig. 3 Hydrocarbon distribution (a) and  $C_{5+}$  composition (b) in the case of  $CO_2$  hydrogenation over CoFe/HZ-5(40) with different proximities; hydrocarbon distribution (c) and  $C_{5+}$  composition (d) of  $CO_2$  hydrogenation over tandem catalysts with different CoFe/HZ-5(40) mass ratios. Reaction conditions:  $320\text{ }^\circ\text{C}$ ,  $3.0\text{ MPa}$ ,  $H_2/CO_2/N_2 = 72/24/4$  (vol%),  $4000\text{ mL g}_{\text{cat}}^{-1}\text{ h}^{-1}$ , time on steam = 14 h.

$0.2$  to  $0.8$ . A CoFe/HZSM-5 mass ratio of  $0.33$  results in the highest  $C_{5+}$  hydrocarbon selectivity at  $71.5\%$ . Likewise, the ratio of olefins to paraffins in the  $C_2-C_4$  hydrocarbon products surges from  $0.3$  to  $5.1$  as the CoFe/HZSM-5 mass ratio increases from  $0.2$  to  $0.8$ . (Fig. 3d). Specifically, at a CoFe/HZ-5(40) mass ratio of  $0.8$ , the content of aromatic hydrocarbons in the  $C_{5+}$  fraction drops to  $15.7\%$ , compared to  $73.1\%$  at a ratio of  $0.33$ . This contrast highlights the zeolite's pivotal role in olefin oligomerization, isomerization, and aromatization.

Furthermore, an investigation was conducted to analyse the impact of temperature and pressure on the system (Fig. S7a and b, ESI†). The  $CO_2$  hydrogenation process involves a series of multi-step reactions,<sup>23</sup> each with potentially different optimal temperatures. Choosing the right reaction temperature is therefore crucial for enhancing the overall performance. The  $CO_2$  conversion rate escalates from  $25.7\%$  to  $50.7\%$  as temperature rises from  $280$  to  $380\text{ }^\circ\text{C}$ .  $CH_4$  and  $C_2-C_4$  hydrocarbon selectivity



initially drops and then rises, bottoming out at 8.7% and 17.1%, respectively, at 320 °C. Conversely, C<sub>5+</sub> hydrocarbon selectivity first increases, then decreases, peaking at 74.3% at 320 °C. The ratio of iso-paraffins to normal paraffins in the C<sub>4</sub> and C<sub>5</sub> fractions (i-C<sub>4</sub>/n-C<sub>4</sub> and i-C<sub>5</sub>/n-C<sub>5</sub>) increases gradually with temperature. This suggests that higher temperature enhances the isomerization ability of HZSM-5. In addition, beyond 320 °C, the composition of iso-paraffins and aromatics in the C<sub>5+</sub> hydrocarbon fraction remains relatively stable despite temperature increases. Based on these findings, it can be concluded that the optimal selectivity for C<sub>5+</sub> hydrocarbons and minimized CH<sub>4</sub> selectivity were observed at 320 °C.

In CO<sub>2</sub> hydrogenation, the RWGS reaction is isovolumetric, while the FTS reaction decreases the volume, making the overall process volume-reducing. Increasing the pressure aids the forward reaction but also complicates the desorption of products from the catalyst surface. Hence, appropriate reaction pressure is critical for performance optimization. Fig. S7c (ESI<sup>†</sup>) reveals that upping the pressure boosts the CO<sub>2</sub> conversion rate from 36.8% to 48.1% and diminishes CO selectivity from 16.3% to 4.7%. This effect suggests that both RWGS and FTS benefit from heightened pressure, with a more pronounced impact on FTS, resulting in accelerated intermediate CO conversion and lower by-product CO selectivity. Moreover, Fig. S7d (ESI<sup>†</sup>) demonstrates the pronounced impact of pressure on hydrocarbon distribution. Specifically, at low pressures, CH<sub>4</sub> selectivity is minimal. However, upon exceeding 3 MPa, CH<sub>4</sub> selectivity notably rises, whereas aromatic selectivity in C<sub>5+</sub> hydrocarbons takes an inverse trajectory. This indicates a reduced favourability for aromatization at higher pressures. Additionally, as pressure rises, i-C<sub>4</sub>/n-C<sub>4</sub> and i-C<sub>5</sub>/n-C<sub>5</sub> ratios decline, pointing to adverse effects on zeolite-mediated isomerization.

The CoFe/HZSM-5 tandem catalyst is a highly effective system for the conversion of CO<sub>2</sub> into C<sub>5+</sub> hydrocarbons. In comparison to the conventional Fe catalyst, the enhanced catalytic activity of the CoFe alloy catalyst facilitates the more efficient conversion of CO<sub>2</sub> to olefins. This heightened efficiency leads to an observed augmentation of intermediate olefins within CoFe/HZ-5(40) as compared to Fe/HZ-5(40), consequently resulting in an increased yield of C<sub>5+</sub> hydrocarbons. The results clearly show that several factors such as the zeolite acidity, the spatial proximity, the mass ratio of CoFe to HZSM-5, and the specific reaction conditions all play significant roles in determining the performance of the catalyst. Optimizing these factors significantly enhances the selectivity towards C<sub>5+</sub> hydrocarbons, contributing to the more effective utilization of CO<sub>2</sub> in the production of valuable hydrocarbons.

This work was supported by the National Key R&D Program of China (2022YFA1504700), National Natural Science Foundation of China (22078315), the Youth Innovation Promotion

Association of the Chinese Academy of Sciences (2020189), the Natural Science Foundation of Liaoning Province (2022-MS-027), and the Youth Science and Technology Star Project Support Program of Dalian City (2021RQ123), DICP (DICP I202012, DICP I202138).

## Conflicts of interest

There are no conflicts to declare.

## Notes and references

- 1 A. Banerjee, G. R. Dick, T. Yoshino and M. W. Kanan, *Nature*, 2016, **531**, 215–219.
- 2 E. E. Benson, C. P. Kubiak, A. J. Sathrum and J. M. Smieja, *Chem. Soc. Rev.*, 2009, **38**, 89–99.
- 3 P. Gao, S. Li, X. Bu, S. Dang, Z. Liu, H. Wang, L. Zhong, M. Qiu, C. Yang, J. Cai, W. Wei and Y. Sun, *Nat. Chem.*, 2017, **9**, 1019–1024.
- 4 P. Gao, S. Dang, S. Li, X. Bu, Z. Liu, M. Qiu, C. Yang, H. Wang, L. Zhong, Y. Han, Q. Liu, W. Wei and Y. Sun, *ACS Catal.*, 2018, **8**, 571–578.
- 5 J. Wei, Q. Ge, R. Yao, Z. Wen, C. Fang, L. Guo, H. Xu and J. Sun, *Nat. Commun.*, 2017, **8**, 15174.
- 6 L. Guo, J. Sun, Q. Ge and N. Tsubaki, *J. Mater. Chem. A*, 2018, **6**, 23244–23262.
- 7 J. Zhu, P. Wang, X. Zhang, G. Zhang, R. Li, W. Li, T. P. Senftle, W. Liu, J. Wang, Y. Wang, A. Zhang, Q. Fu, C. Song and X. Guo, *Sci. Adv.*, 2022, **8**, eabm3629.
- 8 R. E. Owen, J. P. O'Byrne, D. Mattia, P. Plucinski, S. I. Pasco and M. D. Jones, *Chem. Commun.*, 2013, **49**, 11683–11685.
- 9 J. Wei, R. Yao, Q. Ge, D. Xu, C. Fang, J. Zhang, H. Xu and J. Sun, *Appl. Catal., B*, 2021, **283**, 119648.
- 10 J. Wei, R. Yao, Q. Ge, Z. Wen, X. Ji, C. Fang, J. Zhang, H. Xu and J. Sun, *ACS Catal.*, 2018, **8**, 9958–9967.
- 11 G. T. Kokotailo, S. L. Lawton, D. H. Olson and W. M. Meier, *Nature*, 1978, **272**, 437–438.
- 12 A. Ramirez, A. Dutta Chowdhury, M. Caglayan, A. Rodriguez-Gomez, N. Wehbe, E. Abou-Hamad, L. Gevers, S. Ould-Chikh and J. Gascon, *Catal. Sci. Technol.*, 2020, **10**, 1507–1517.
- 13 E. M. Flanigen, J. M. Bennett, R. W. Grose, J. P. Cohen, R. L. Patton, R. M. Kirchner and J. V. Smith, *Nature*, 1978, **271**, 512–516.
- 14 Y. Li, L. Li and J. Yu, *Chem*, 2017, **3**, 928–949.
- 15 N. Liu, J. Wei, J. Xu, Y. Yu, J. Yu, Y. Han, K. Wang, J. I. Oregre, Q. Ge and J. Sun, *Appl. Catal., B*, 2023, **328**, 122476.
- 16 L. Zhang, Y. Dang, X. Zhou, P. Gao, A. Petrus van Bavel, H. Wang, S. Li, L. Shi, Y. Yang, E. I. Vovk, Y. Gao and Y. Sun, *The Innovation*, 2021, **2**, 100170.
- 17 Z. Zeng, Z. Li, L. Kang, X. Han, Z. Qi, S. Guo, J. Wang, A. Rykov, J. Lv, Y. Wang and X. Ma, *ACS Catal.*, 2022, **12**, 6016–6028.
- 18 K. Y. Kim, H. Lee, W. Y. Noh, J. Shin, S. J. Han, S. K. Kim, K. An and J. S. Lee, *ACS Catal.*, 2020, **10**, 8660–8671.
- 19 Q. Yang, V. A. Kondratenko, S. A. Petrov, D. E. Doronkin, E. Saraçi, H. Lund, A. Arinchtin, R. Kraehnert, A. S. Skrypnik, A. A. Matvienko and E. V. Kondratenko, *Angew. Chem., Int. Ed.*, 2022, **61**, e202116517.
- 20 Z. Wan, W. Wu, G. Li, C. Wang, H. Yang and D. Zhang, *Appl. Catal., A*, 2016, **523**, 312–320.
- 21 Y. Ni, Z. Chen, Y. Fu, Y. Liu, W. Zhu and Z. Liu, *Nat. Commun.*, 2018, **9**, 3457.
- 22 J. Liu, A. Zhang, X. Jiang, M. Liu, J. Zhu, C. Song and X. Guo, *Ind. Eng. Chem. Res.*, 2018, **57**, 9120–9126.
- 23 A. Dokania, A. Ramirez, A. Bavykina and J. Gascon, *ACS Energy Lett.*, 2019, **4**, 167–176.

